Floquet Cavity Electromagnonics

Jing Xu,[1] Changchun Zhong,[2] Xu Han,[1] Dafei Jin,[1] Liang Jiang,[2] and Xufeng Zhang[1,*]
[1]Center for Nanoscale Materials, Argonne National Laboratory, Lemont, Illinois 60439, USA
[2]Pritzker School of Molecular Engineering, University of Chicago, Chicago, Illinois 60637, USA

(Received 9 July 2020; revised 12 September 2020; accepted 26 October 2020; published 1 December 2020)

Hybrid magnonics has recently attracted intensive attention as a promising platform for coherent information processing. In spite of its rapid development, on-demand control over the interaction of magnons with other information carriers, in particular, microwave photons in electromagnonic systems, has been long missing, significantly limiting the potential broad applications of hybrid magnonics. Here, we show that, by introducing Floquet engineering into cavity electromagnonics, coherent control on the magnon-microwave photon coupling can be realized. Leveraging the periodic temporal modulation from a Floquet drive, our first-of-its-kind Floquet cavity electromagnonic system enables the manipulation of the interaction between hybridized cavity electromagnonic modes. Moreover, we have achieved a new coupling regime in such systems: the Floquet ultrastrong coupling, where the Floquet splitting is comparable with or even larger than the level spacing of the two interacting modes, beyond the conventional rotating-wave picture. Our findings open up new directions for magnon-based coherent signal processing.

DOI: 10.1103/PhysRevLett.125.237201

Introduction.—Floquet engineering, which refers to temporal modulation of system parameters by periodic drives, has been known as an effective approach for controlling the dynamics of a given system. In recent years, it has been implemented in a large variety of systems ranging from cold atoms [1–6] and quantum dots [7,8] to integrated photonics [9] and Josephson junction devices [10,11], enabling a diverse variety of novel functionalities. Aside from practical applications, Floquet-driven systems have also significantly advanced fundamental research, leading to the experimental observation of novel non-equilibrium phenomena such as discrete time-crystalline phases [12–14] or Floquet spin-glass phases [15].

Among all coherent information systems, magnonic systems have been emerging as a highly promising platform because of their unique properties. In magnonic systems, magnons—quasiparticles of spin waves—are used as the information carrier. Their coherent interactions with a broad variety of other systems have been demonstrated recently [16–27]. For instance, magnons, with their frequencies in the gigahertz range, naturally interact with microwave photons through magnetic dipole-dipole interactions. Most importantly, the coupling strength is significantly enhanced by the large spin density in the magnon medium and can reach the strong coupling regime. As of today, such hybrid cavity electromagnonic systems have been experimentally demonstrated in both classical [16–19,26,27] and quantum [28–30] regimes, becoming the most intensively studied hybrid magnonic systems. With unique magnon properties such as large tunability and time reversal symmetry breaking, novel functionalities can be achieved in these systems [31–35].

However, unlike in systems such as optomechanics [36–40] that employ parametric coupling, the direct magnon-photon coupling in a given hybrid electromagnonic system is usually difficult to manipulate. Although magnons naturally possess great tunability, fast tuning of the coupling is extremely hard to achieve, making the dynamic control of coherent signals highly challenging. This poses a tremendous obstacle in the broad applications of hybrid electromagnonics. In this Letter, we show that, by introducing Floquet engineering into cavity electromagnonics, *in situ* tuning of the magnon-photon interaction is, to the best of our knowledge, achieved for the first time. In our Floquet cavity electromagnonic system, a driving field induces mode splitting that is analogous to the Autler-Townes splitting (ATS) in atomic physics, where the coupling strength between two energy levels is determined by the strength of the Floquet driving field. The system response is studied in both the frequency and temporal domains. More interestingly, our system supports a new coupling regime—Floquet ultrastrong coupling (FUSC), which has not been observed previously in existing Floquet systems. In this regime, the mode splitting exceeds the energy level spacing of the two interacting modes, distinguishing it from the conventional ultrastrong coupling where the coupling strength is a significant fraction of the bare frequencies of the uncoupled systems. We further show that, in this regime, the rotating-wave approximation (RWA) no longer holds and the counterrotating terms in the Hamiltonian start to exhibit non-negligible effects on the system response. All these findings point to a new direction for advancing magnon-based coherent information processing.

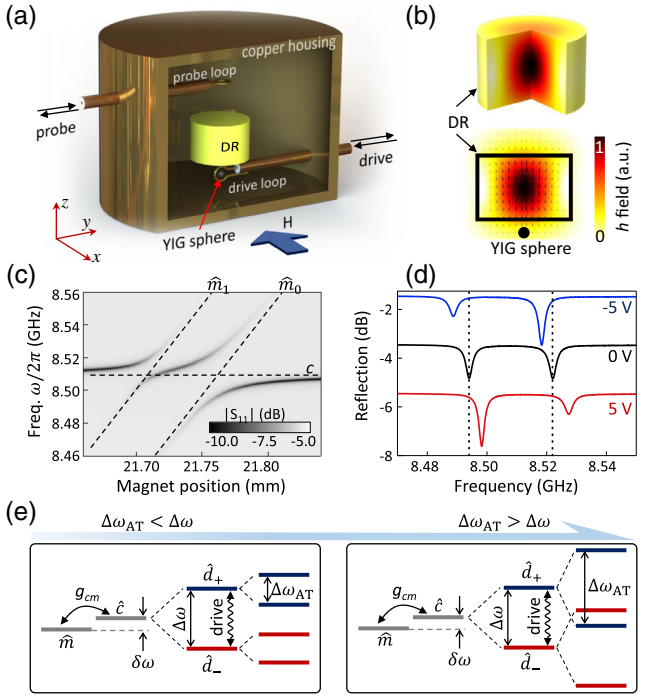

FIG. 1. (a) Device schematics. A YIG sphere is placed underneath a dielectric resonator inside a copper housing, with a bias magnetic field H along x direction. The coaxial probe loop is for microwave excitation and readout; the drive loop provides the Floquet driving field along x. (b) Simulated magnetic components (h field) of the cavity field for the $TE_{01\delta}$ mode of the dielectric resonator. Color, field intensity; arrows, field direction. (c) Measured cavity reflection at various magnetic fields (controlled by magnet position). Two avoided crossings correspond to the strong coupling between the cavity photon mode ($\hat{c}$) and two magnon modes ($\hat{m}_0$ and $\hat{m}_1$). Freq., frequency. (d) Cavity reflection measured at $x = 21.75$ mm with different dc bias conditions applied to the drive loop. Curves are shifted vertically for clarity. (e) Energy level diagram. $\hat{m}$, magnon mode; $\hat{c}$, microwave photon mode; $\delta\omega$, magnon detuning; g_{cm}, magnon-photon coupling strength; $\hat{d}_{\pm}$, upper (lower) hybrid mode; $\Delta\omega$, energy separation between two hybrid modes; $\Delta\omega_{AT}$, Autler-Townes splitting. A driving field is applied to enable the transition between hybrid modes $\hat{d}_-$ and $\hat{d}_+$.

System description.—Our system [Fig. 1(a)] consists of a cylindrical dielectric resonator (DR) supporting a transverse electric mode $TE_{01\delta}$ at $\omega_c = 2\pi \times 8.5$ GHz with its microwave magnetic fields along z [Fig. 1(b)]. The DR is hosted inside a copper housing to eliminate radiation losses. Together with its low dielectric loss, it supports resonances with quality factors as high as 10 000 at room temperature (see Supplemental Material [41]). A loop antenna is placed above the DR with its loop along z direction to excite and probe the cavity photon mode.

An yttrium iron garnet (YIG) sphere is placed close to the bottom surface of the DR. With a permanent magnet outside the cavity housing to provide a bias magnetic field at a strength H, the YIG sphere supports a uniform magnon mode at frequency $\omega_m = \gamma H$, where $\gamma \approx 2\pi \times 28$ GHz/T is the gyromagnetic ratio. The bias field is applied perpendicular to z (along x) to maximize the interaction between magnons and cavity photons [16]. By changing the x position of the bias magnet, the bias field strength can be changed, which in turn tunes the magnon frequency.

The system is described by the Hamiltonian

$$\hat{H} = \hbar\omega_c \hat{c}^\dagger \hat{c} + \hbar\omega_m \hat{m}^\dagger \hat{m} + \hbar g_{cm}(\hat{c}^\dagger \hat{m} + \hat{c}\hat{m}^\dagger) + \hat{H}_F, \quad (1)$$

where $\hbar$ is the reduced Planck's constant, $\hat{c}^\dagger$ and $\hat{c}$ ($\hat{m}^\dagger$ and $\hat{m}$) are the creation and annihilation operators for the cavity photon (magnon) mode, g_{cm} is the beam-splitter-type coupling strength, and $\hat{H}_F$ is the Floquet driving term. Under strong coupling condition $g_{cm} > \kappa_c/2, \kappa_m/2$, where κ_c and κ_m represent the energy dissipation rates of the cavity photon and magnon mode, respectively, the two modes hybridize and coherent information conversion is enabled. This condition is confirmed by the extracted coupling strength $g_{cm} = 2\pi \times 14.0$ MHz, which largely exceeds both $\kappa_c/2 = 2\pi \times 1.0$ and $\kappa_m/2 = 2\pi \times 2.2$ MHz [41]. Strong coupling is also evident from the avoided-crossing features in the cavity reflection spectra measured when ω_m is swept [Fig. 1(c)], even though backgrounds such as cable losses are not removed from the data. Although two magnon modes $\hat{m}_0$ and $\hat{m}_1$ are observed, only $\hat{m}_0$ will be used in the discussion hereafter.

Floquet driving is realized in our system through frequency modulation of the magnon mode. A small coil, which has previously been used only for gigahertz readout or control [44], is looped tightly around the YIG sphere to modulate the bias magnetic field (see Supplemental Material [41]). The loop is aligned along the bias field direction (x direction) and has only three turns to reduce the inductance to ensure fast modulation. The effect of the driving coil is confirmed by the shifted magnon resonances when dc drives are applied [Fig. 1(d)]. With a sinusoidal drive, the Floquet term of the Hamiltonian reads

$$\hat{H}_F = \hbar\Omega \hat{m}^\dagger \hat{m} \cos(\omega_D t), \quad (2)$$

where Ω and ω_D are the strength and frequency of the driving field, respectively.

Magnonic Autler-Townes effect.—When the magnon and photon modes are on resonance ($\delta\omega = \omega_m - \omega_c = 0$), two hybrid modes $\hat{d}_\pm = (\hat{c} \pm \hat{m})/\sqrt{2}$ form at frequencies $\omega_\pm = \omega_c \pm g_{cm}$. Using $\hat{d}_\pm$ as the new basis and applying RWA [41], the system Hamiltonian can be rewritten as

$$\hat{H}_{RWA} = \frac{\delta\omega_D}{2}\hat{d}_-^\dagger \hat{d}_- - \frac{\delta\omega_D}{2}\hat{d}_+^\dagger \hat{d}_+ + \frac{\Omega}{4}(\hat{d}_-^\dagger \hat{d}_+ + \hat{d}_- \hat{d}_+^\dagger), \quad (3)$$

where $\delta\omega_D = \Delta\omega - \omega_D$. Here $\Delta\omega = \omega_+ - \omega_- = 2g_{cm}$ is the level spacing between the two hybrid modes. This Hamiltonian shows that the Floquet field drives the transition between the two hybrid modes. As a result, each

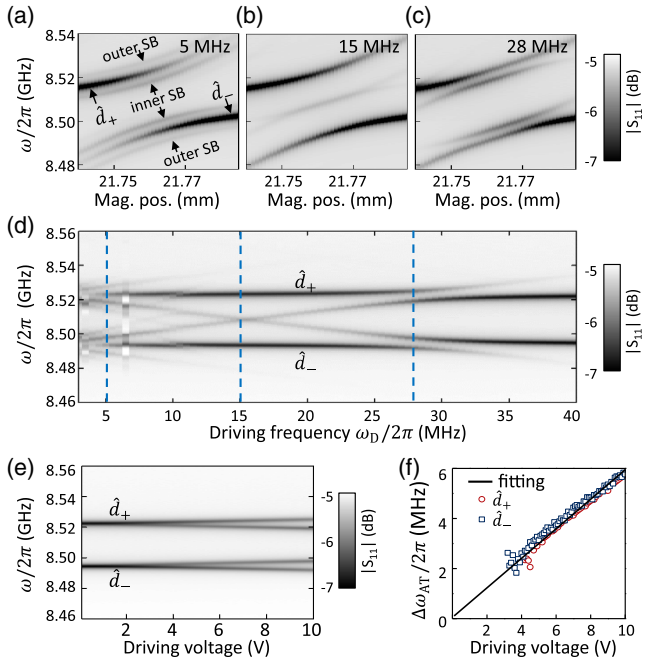

FIG. 2. (a)–(c) Measured cavity reflection ($|S_{11}|$) spectra versus the bias magnetic field at a 10-V peak-to-peak driving amplitude for three frequencies: $\omega_D = 2\pi \times 5, 15, 28$ MHz, respectively. In addition to the avoided crossing caused by the strong coupling between the cavity photon mode ($\hat{c}$) and magnon mode ($\hat{m}_0$), sidebands are created by the ac driving fields. (d) Measured cavity reflection spectra as a function of driving frequency at $x = 21.762$ mm when $\delta\omega = 0$. The dashed lines correspond to conditions for (a)–(c). (e) Measured cavity reflection spectra as a function of driving amplitude, with $\delta\omega = 0$ and $\omega_D = 2\pi \times 28$ MHz. (f) Extracted Autler-Townes splitting ($\Delta\omega_{\mathrm{AT}}$) for both $\hat{d}_-$ (square), $\hat{d}_+$ (circle) modes in (e) as a function of the driving voltage. Solid line is from the numerical fitting. SB, sideband; Mag. pos., magnet position.

hybrid mode splits into two energy levels with a spacing $\Delta\omega_{\mathrm{AT}}$ that is determined by the driving strength, resembling the ATS in a laser-driven two-level system [Fig. 1(e)].

The cavity responses under a Floquet drive are plotted in Figs. 2(a)–2(c), which are enlarged to show the avoided crossing between the magnon ($\hat{m}_0$) and cavity ($\hat{c}$) modes. Two hybrid modes ($\hat{d}_\pm$) are visible, each with two sidebands created by the Floquet drive. As the driving frequency ω_D increases, the inner sideband of one hybrid mode approaches the other hybrid mode, eventually leading to the ATS when $\omega_D = \Delta\omega = 2\pi \times 28$ MHz [Fig. 2(c)].

The on-resonance ($\delta\omega = 0$) response of the system as a function of the driving frequency is shown in Fig. 2(d). The most prominent feature is that the upper (lower) sideband of $\hat{d}_-$ ($\hat{d}_+$) mode moves closer to the other mode $\hat{d}_+$ ($\hat{d}_-$) as the driving frequency increases and eventually crosses that mode with an avoided-crossing feature at $\omega_D = \Delta\omega = 2\pi \times 28$ MHz, which corresponds to the ATS. Although the modulation creates two sidebands for each hybrid mode at $\omega_\pm \pm \omega_D$, the lower (upper) sideband for $\hat{d}_-$ ($\hat{d}_+$) rapidly disappears as ω_D increases because it does not couple with the other hybrid mode. Note that all these features are independent of the phase of the Floquet drive [41].

Analogous to laser-driven two-level systems, the ATS observed in our system is also determined by the driving strength Ω, which is controlled by the signal voltage sent into the driving coil in our experiment. A larger driving strength results in a wider ATS, as shown in Fig. 2(e), where the on-resonance cavity reflection is plotted as a function of the driving voltage at a driving frequency $\omega_D = 2\pi \times 28$ MHz. According to Eq. (3), the ATS is linearly proportional to the driving strength: $\Delta\omega_{\mathrm{AT}} = \Omega/2$. This is confirmed by the numerical fitting of the extracted ATS [Fig. 2(f)].

In addition to modifying the equilibrium spectra, the Floquet drive also opens up new possibilities for manipulating the electromagnonic dynamics, which has been a grand challenge limiting most of previous demonstrations to quasistatic controls [16,34,45]. Figures 3(a) and 3(c) plot the measured and calculated cavity reflection signals after a 20-ns-wide rectangular microwave pulse centered

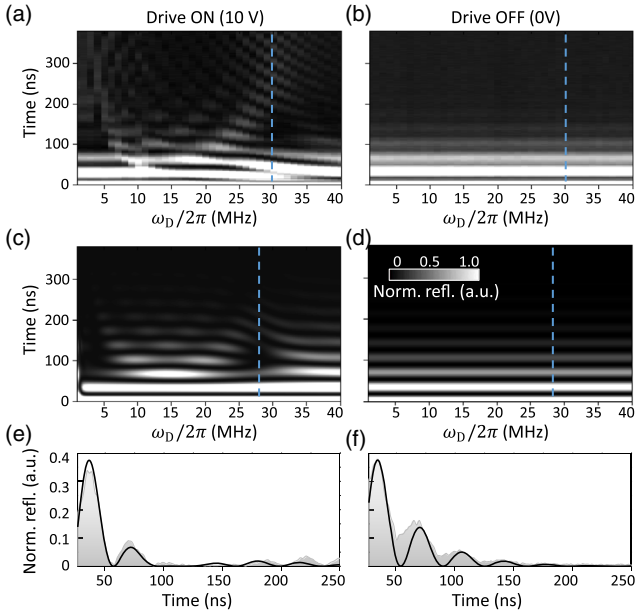

FIG. 3. (a),(b) Measured cavity temporal response under different driving frequencies after a rectangular pulsed excitation (center frequency, $2\pi \times 8.52$ GHz; width, 20 ns; peak-to-peak amplitude, 10 V) at time zero when the Floquet drive is on and off, respectively. (c),(d) Calculated cavity temporal response with and without the Floquet drive, respectively. (e),(f) Enlarged line plot of the theoretical (solid line) and experimental (grayed area) temporal responses at Floquet driving frequencies as indicated by the vertical dashed lines in (a)–(d) ($\omega_D = 2\pi \times 28$ MHz for the theoretical calculation, while $\omega_D = 2\pi \times 31$ MHz for experiment results, which is slightly higher because of magnon nonlinearity effects induced by the strong microwave input) with and without the Floquet drive, respectively. Norm. refl., normalized reflection.

at $2\pi \times 8.52$ GHz is sent into the cavity (see Supplemental Material [41]). Since the cavity reflection is proportional to the amplitude of the electromagnetic field inside the cavity, it reveals the dynamics of cavity photons such as their dissipation (exponential decay envelops in the reflection) and the coherent energy exchange with magnons (periodic oscillations). At low driving frequencies where the Floquet effect is weak because $\omega_D \neq \Delta\omega$, the system dynamics is dominated by the intrinsic magnon-photon coupling which leads to Rabi-like oscillations with a period $T = 2\pi/2g_{cm} = 36$ ns. This is more clearly visible when the Floquet drive is completely turned off [Figs. 3(b) and 3(d)], and it is evident that the amplitude of the oscillating signal monotonically decreases as a result of dissipation. When the Floquet drive is turned on and, in particular, when the driving frequency matches the spacing between the two hybrid modes ($\omega_D = \omega_+ - \omega_- = 2\pi \times 28$ MHz), coherent coupling between the hybrid modes is enabled and, consequently, the temporal response of the system is substantially modified. As shown in Fig. 3(e), the oscillation amplitude first rapidly decays into a minimum at around 120 ns and then increases again at around 200 ns, with the time interval matching the ATS ($2\pi/2\Delta\omega_{\mathrm{AT}} \approx 80$ ns for a 10-V Floquet drive). Note that in the time-domain measurements the cavity dissipation becomes larger ($\kappa_c = 2\pi \times 4.2$ MHz) because the external coupling rate is adjusted to optimize the reflected signal, which agrees with the exponential decay rate in Fig. 3(f). Since such Floquet-drive-induced coherent interaction can be controlled by the amplitude of the drive, it provides new opportunities for complex real-time manipulations of the magnon-photon coupling using electrical pulses.

Floquet ultrastrong coupling.—In the above analysis, the Floquet drive is relatively weak, yielding small ATS $\Delta\omega_{\mathrm{AT}} < \Delta\omega$. However, in the strong-drive regime where the ATS is comparable with or even larger than the level spacing between $\hat{d}_\pm$ ($\Delta\omega_{\mathrm{AT}} \gtrsim \Delta\omega$), the RWA Hamiltonian in Eq. (3) is no longer sufficient to describe the system. This corresponds to a novel coupling regime: the FUSC regime. Here, the counterrotating terms need to be included [41] and the Hamiltonian becomes

$$\hat{H} = \omega_- \hat{d}_-^\dagger \hat{d}_- + \omega_+ \hat{d}_+^\dagger \hat{d}_+ + g_{cm} \sum_{n=\mathrm{odd}}^{\infty} J_n\left(\frac{\Omega}{\omega_D}\right)[\hat{d}_-^\dagger \hat{d}_+ e^{i(n\omega_D t)} + \hat{d}_- \hat{d}_+^\dagger e^{-i(n\omega_D t)}], \tag{4}$$

where n is the sideband order, and $J_n(x)$ is the nth Bessel function of the first kind.

The last term in Eq. (4) is the summation of interactions between different sidebands of $\hat{d}_\pm$ modes. The Floquet drive generates a series of sidebands at frequencies $\omega_\pm \pm n\omega_D$. Multiple sidebands and their interactions with the other hybrid mode are clearly visible in Fig. 2(d) when ω_D is small. Specifically, the individual coupling strength of the nth sideband of mode $\hat{d}_\pm$ with mode $\hat{d}_\mp$ is determined as $g_n = g_{cm} J_n(\Omega/\omega_D)$. Apparently, this coupling strength is determined by the intrinsic magnon-photon coupling strength g_{cm}, but can be controlled by the frequency and strength of the Floquet drive. Interestingly, only sidebands with odd n values have nonzero coupling strengths. This is confirmed by the experimental observation in Fig. 2(d), where only the first and third sidebands of $\hat{d}_\pm$ cross $\hat{d}_\mp$ with an avoided crossing (at $2\pi \times 28$ and $2\pi \times 11$ MHz, respectively), while the second sideband does not. The vanished coupling strength for even sidebands can be explained by the cancellation of the coupling strengths via different coupling paths (see Supplemental Material [41]). When the Floquet drive is relatively small, the ATS can be determined as $\Delta\omega_{\mathrm{AT}} = 2g_n$. But this does not apply for strong drives, where the effects from multiple sidebands need to be considered.

In general, experimental investigation of the strong-drive regime is very challenging because the maximally achievable driving strength is limited. Alternatively, it can be achieved by reducing the level spacing $\Delta\omega$ to make it comparable with or smaller than the ATS $\Delta\omega_{\mathrm{AT}}$. This is realized with a reduced intrinsic magnon-photon coupling strength g_{cm} by increasing the gap between the YIG sphere and the DR surface. Figure 4(a) shows the measured cavity reflection spectra as a function of the driving frequency with a reduced magnon-photon coupling strength $g_{cm} = 2\pi \times 1.825$ MHz, where ATS is observed at $\omega_D = 2g_{cm} = 2\pi \times 3.650$ MHz for both $\hat{d}_-$ and $\hat{d}_+$. This

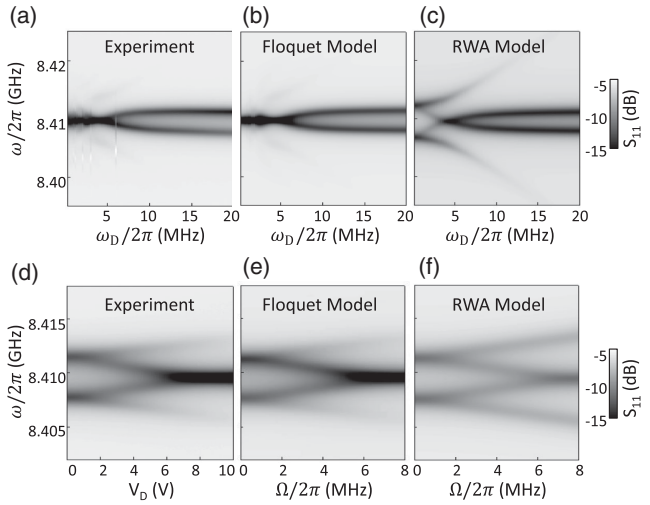

FIG. 4. (a)–(c) Cavity reflection spectra when the driving frequency ω_D is swept at a fixed driving amplitude (10 V peak to peak), obtained from experiment, Floquet model, and RWA model, respectively. (d)–(f) Cavity reflection spectra when the driving amplitude is swept at a fixed driving frequency ($\omega_D = 2\pi \times 3.85$ MHz), obtained from experiment, Floquet model, and RWA model, respectively.

agrees with the results calculated using the Floquet scattering matrix derived from the full Hamiltonian in Eq. (1), as shown in Fig. 4(b). As a comparison, the calculated cavity reflection spectra based on the Hamiltonian with RWA in Eq. (3) are plotted in Fig. 4(c), which exhibit severe deviation from the experimental results, showing the significant effects of the counterrotating terms.

Similarly, the measured cavity reflection spectra under different driving strengths are plotted in Fig. 4(d), which match the theory calculations based on the full Floquet Hamiltonian [Fig. 4(e)] and largely deviate from the calculations using RWA [Fig. 4(f)]. Compared with the RWA results, the RWA breaking has two major effects: first, the outer two branches become much weaker than the inner two branches in both ω_D- [Figs. 4(a)–4(c)] and Ω-dependent [Figs. 4(d)–4(f)] cavity reflections; second, the inner two branches merge and form a much deeper dip. These spectral features are attributed to the fact that multiple driving photons (in contrast to a single photon for weak drives) are involved in the interaction between a $\hat{d}_-$ and a $\hat{d}_+$ excitation in the FUSC regime.

Conclusion.—To conclude, this Letter demonstrates a Floquet cavity electromagnonic system that provides controllable hybridization between magnons and microwave photons. The Floquet engineering technique provides a versatile approach for manipulating hybrid magnon states and enables the observation of on-demand ATS. The measurement results in both the frequency and temporal domains agree with our Floquet driving model and the corresponding scattering matrix. More importantly, this approach leads to a new coupling regime—FUSC—for hybrid magnonics, where RWA breaks down and new phenomena are observed. This technique can be readily applied as a general approach to a broad range of magnonic systems that have been lacking the essential controllability, producing not only new functionalities but also novel nonequilibrium magnon dynamics. For instance, more complicated spectral control can be obtained if the driving strength can be further enhanced. Besides, temporal manipulations such as Rabi or Ramsey pulse sequences will be allowed, in particular, when system parameters such as dissipation rates and driving strength are further optimized, enabling practical applications such as mode swapping or storage [9]. It is worth noting that such a Floquet driving scheme is not exclusive for our dielectric resonator but can be generalized to various cavity electromagnonic systems. Although our experiments are carried out at room temperature in the classical regime, the principles demonstrated here also directly apply to quantum operations, where hybrid magnonics has shown great potentials for applications such as quantum transduction [46–49].

This work was performed, in part, at the Center for Nanoscale Materials, a U.S. Department of Energy Office of Science User Facility, and supported by the U.S. Department of Energy, Office of Science, under Contract No. DE-AC02-06CH11357. L. J. acknowledges support from the ARL-CDQI (W911NF-15-2-0067), ARO (W911NF-18-1-0020, W911NF-18-1-0212), ARO MURI (W911NF-16-1-0349), AFOSR MURI (FA9550-15-1-0015, FA9550-19-1-0399), NSF (EFMA-1640959, OMA-1936118), and the Packard Foundation (2013-39273).

*xufeng.zhang@anl.gov

[1] A. Eckardt, Rev. Mod. Phys. **89**, 011004 (2017).
[2] J. Eisert, M. Friesdorf, and C. Gogolin, Nat. Phys. **11**, 124 (2015).
[3] H. Lignier, C. Sias, D. Ciampini, Y. Singh, A. Zenesini, O. Morsch, and E. Arimondo, Phys. Rev. Lett. **99**, 220403 (2007).
[4] L. Jiang, T. Kitagawa, J. Alicea, A. R. Akhmerov, D. Pekker, G. Refael, J. I. Cirac, E. Demler, M. D. Lukin, and P. Zoller, Phys. Rev. Lett. **106**, 220402 (2011).
[5] I.-D. Potirniche, A. C. Potter, M. Schleier-Smith, A. Vishwanath, and N. Y. Yao, Phys. Rev. Lett. **119**, 123601 (2017).
[6] J.-R. Li, B. Shteynas, and W. Ketterle, Phys. Rev. A **100**, 033406 (2019).
[7] J. Stehlik, Y.-Y. Liu, C. Eichler, T. R. Hartke, X. Mi, M. J. Gullans, J. M. Taylor, and J. R. Petta, Phys. Rev. X **6**, 041027 (2016).
[8] J. V. Koski, A. J. Landig, A. Palyi, P. Scarlino, C. Reichl, W. Wegscheider, G. Burkard, A. Wallraff, K. Ensslin, and T. Ihn, Phys. Rev. Lett. **121**, 043603 (2018).
[9] M. Zhang, C. Wang, Y. Hu, A. Shams-Ansari, T. Ren, S. Fan, and M. Loncar, Nat. Photonics **13**, 36 (2019).
[10] M. Sameti and M. J. Hartmann, Phys. Rev. A **99**, 012333 (2019).
[11] X. Wang, H.-R. Li, and F.-L. Li, New J. Phys. **22**, 033037 (2020).
[12] J. Zhang, P. W. Hess, A. Kyprianidis, P. Becker, A. Lee, J. Smith, G. Pagano, I.-D. Potirniche, A. C. Potter, A. Vishwanath, N. Y. Yao, and C. Monroe, Nature (London) **543**, 217 (2017).
[13] S. Choi, J. Choi, R. Landig, G. Kucsko, H. Zhou, J. Isoya, F. Jelezko, S. Onoda, H. Sumiya, V. Khemani, C. von Keyserlingk, N. Y. Yao, E. Demler, and M. D. Lukin, Nature (London) **543**, 221 (2017).
[14] Z. Gong, R. Hamazaki, and M. Ueda, Phys. Rev. Lett. **120**, 040404 (2018).
[15] E. P. Raposo, I. R. R. Gonzalez, A. M. S. Macedo, B. C. Lima, R. Kashyap, L. S. Menezes, and A. S. L. Gomes, Phys. Rev. Lett. **122**, 143903 (2019).
[16] X. Zhang, C.-L. Zou, L. Jiang, and H. X. Tang, Phys. Rev. Lett. **113**, 156401 (2014).
[17] Y. Tabuchi, S. Ishino, T. Ishikawa, R. Yamazaki, K. Usami, and Y. Nakamura, Phys. Rev. Lett. **113**, 083603 (2014).
[18] M. Goryachev, W. G. Farr, D. L. Creedon, Y. Fan, M. Kostylev, and M. E. Tobar, Phys. Rev. Applied **2**, 054002 (2014).
[19] L. Bai, M. Harder, Y. P. Chen, X. Fan, J. Q. Xiao, and C.-M. Hu, Phys. Rev. Lett. **114**, 227201 (2015).
[20] X. Zhang, C.-L. Zou, L. Jiang, and H. X. Tang, Sci. Adv. **2**, e1501286 (2016).

[21] X. Zhang, N. Zhu, C.-L. Zou, and H. X. Tang, Phys. Rev. Lett. **117**, 123605 (2016).
[22] A. Osada, R. Hisatomi, A. Noguchi, Y. Tabuchi, R. Yamazaki, K. Usami, M. Sadgrove, R. Yalla, M. Nomura, and Y. Nakamura, Phys. Rev. Lett. **116**, 223601 (2016).
[23] J. A. Haigh, A. Nunnenkamp, A. J. Ramsay, and A. J. Ferguson, Phys. Rev. Lett. **117**, 133602 (2016).
[24] S. Sharma, Y. M. Blanter, and G. E. W. Bauer, Phys. Rev. B **96**, 094412 (2017).
[25] J. Graf, H. Pfeifer, F. Marquardt, and S. Viola Kusminskiy, Phys. Rev. B **98**, 241406(R) (2018).
[26] J. T. Hou and L. Liu, Phys. Rev. Lett. **123**, 107702 (2019).
[27] Y. Li, T. Polakovic, Y.-L. Wang, J. Xu, S. Lendinez, Z. Zhang, J. Ding, T. Khaire, H. Saglam, R. Divan, J. Pearson, W.-K. Kwok, Z. Xiao, V. Novosad, A. Hoffmann, and W. Zhang, Phys. Rev. Lett. **123**, 107701 (2019).
[28] Y. Tabuchi, S. Ishino, A. Noguchi, T. Ishikawa, R. Yamazaki, K. Usami, and Y. Nakamura, Science **349**, 405 (2015).
[29] D. Lachance-Quirion, Y. Tabuchi, S. Ishino, A. Noguchi, T. Ishikawa, R. Yamazaki, and Y. Nakamura, Sci. Adv. **3**, e1603150 (2017).
[30] D. Lachance-Quirion, S. P. Wolski, Y. Tabuchi, S. Kono, K. Usami, and Y. Nakamura, Science **367**, 425 (2020).
[31] X. Zhang, C.-L. Zou, N. Zhu, F. Marquardt, L. Jiang, and H. X. Tang, Nat. Commun. **6**, 8914 (2015).
[32] X. Zhang, A. Galda, X. Han, D. Jin, and V. M. Vinokur, Phys. Rev. Applied **13**, 044039 (2020).
[33] Y.-P. Wang, J. W. Rao, Y. Yang, P.-C. Xu, Y. S. Gui, B. M. Yao, J. Q. You, and C.-M. Hu, Phys. Rev. Lett. **123**, 127202 (2019).
[34] X. Zhang, K. Ding, X. Zhou, J. Xu, and D. Jin, Phys. Rev. Lett. **123**, 237202 (2019).
[35] H. Y. Yuan, P. Yan, S. Zheng, Q. Y. He, K. Xia, and M.-H. Yung, Phys. Rev. Lett. **124**, 053602 (2020).
[36] M. Li, W. H. P. Pernice, C. Xiong, T. Baehr-Jones, M. Hochberg, and H. X. Tang, Nature (London) **456**, 480 (2008).
[37] S. Weis, R. Riviere, S. Deleglise, E. Gavartin, O. Arcizet, A. Schliesser, and T. J. Kippenberg, Science **330**, 1520 (2010).
[38] A. H. Safavi-Naeini, T. P. M. Alegre, J. Chan, M. Eichenfield, M. Winger, Q. Lin, J. T. Hill, D. E. Chang, and O. Painter, Nature (London) **472**, 69 (2011).
[39] J. D. Teufel, T. Donner, D. Li, J. W. Harlow, M. S. Allman, K. Cicak, A. J. Sirois, J. D. Whittaker, K. W. Lehnert, and R. W. Simmonds, Nature (London) **475**, 359 (2011).
[40] M. Aspelmeyer, T. J. Kippenberg, and F. Marquardt, Rev. Mod. Phys. **86**, 1391 (2014).
[41] See Supplemental Material at http://link.aps.org/supplemental/10.1103/PhysRevLett.125.237201 for more theory and experimental details, which includes Refs. [42,43].
[42] J. H. Shirley, Phys. Rev. **138**, B979 (1965).
[43] Given any matrix $\mathbf{A}$ and $\mathbf{B}$, we have $(\mathbf{A}-\mathbf{B})^{-1} = \sum_{k=1}^{\infty}(\mathbf{A}^{-1}\mathbf{B})^{k}\mathbf{A}^{-1}$.
[44] I. Boventer, M. Klaui, R. Macedo, and M. Weides, New J. Phys. **21**, 125001 (2019).
[45] D. Zhang, X.-Q. Luo, Y.-P. Wang, T.-F. Li, and J. Q. You, Nat. Commun. **8**, 1368 (2017).
[46] N. Lauk, N. Sinclair, S. Barzanjeh, J. Covey, M. Saffman, M. Spiropulu, and C. Simon, Quantum Sci. Technol. **5**, 020501 (2020).
[47] D. Lachance-Quirion, Y. Tabuchi, A. Gloppe, K. Usami, and Y. Nakamura, Appl. Phys. Express **12**, 070101 (2019).
[48] R. Hisatomi, A. Osada, Y. Tabuchi, T. Ishikawa, A. Noguchi, R. Yamazaki, K. Usami, and Y. Nakamura, Phys. Rev. B **93**, 174427 (2016).
[49] N. Zhu, X. Zhang, X. Han, C. Zou, C. Zhong, C. Wang, L. Jiang, and H. Tang, Optica **7**, 1291 (2020).